The Astrophysical Journal, 866:124 (9pp), 2018 October 20 https://doi.org/10.3847/1538-4357/aadd0d

Coronal Properties of *Swift*/BAT-selected Seyfert 1 AGNs Observed with *NuSTAR*

N. Kamraj[1], F. A. Harrison[1], M. Baloković[2], A. Lohfink[3], and M. Brightman[1]
[1] Cahill Center for Astronomy and Astrophysics, California Institute of Technology, Pasadena, CA 91125, USA; nkamraj@caltech.edu
[2] Harvard-Smithsonian Center for Astrophysics, 60 Garden Street, Cambridge, MA 02138, USA
[3] Department of Physics, Montana State University, 211 Montana Hall, Bozeman, MT 59717, USA
Received 2018 April 20; revised 2018 August 23; accepted 2018 August 24; published 2018 October 19

Abstract

The *NuSTAR* observatory, with its high sensitivity in hard X-rays, has enabled detailed broadband modeling of the X-ray spectra of active galactic nuclei (AGNs), thereby allowing constraints to be placed on the high-energy cutoff of the X-ray coronal continuum. We investigate the spectral properties of a sample of 46 *NuSTAR*-observed Seyfert 1 AGNs selected from the *Swift*/Burst Alert Telescope 70 month hard X-ray survey. Our measurements of the high-energy cutoff of the continuum from modeling the *NuSTAR* X-ray spectra are used to map out the temperature–compactness (θ–l) plane for AGN coronae. We find that most of the coronae lie clustered near the boundary for runaway pair production, suggesting that annihilation and pair production act to regulate the temperature of the corona. We discuss the implications of coronae whose high-energy cutoff may indicate a low coronal temperature on the heating and thermalization mechanisms in the corona.

Key words: black hole physics – galaxies: active – X-rays: galaxies

1. Introduction

The continuum X-ray emission from active galactic nuclei (AGNs) is believed to originate in a hot, compact corona located above the accretion disk (e.g., Haardt & Maraschi 1993). Compton upscattering of UV and optical photons from the inner accretion disk by coronal electrons produce a power-law-like X-ray continuum, with a cutoff at energies determined by the electron temperature T_e (e.g., Rybicki & Lightman 1979; Zdziarski et al. 2000). The shape of the coronal continuum is sensitive to properties such as the seed photon field, electron temperature, optical depth, and observer viewing angle. The observed rapid variability of the 2–10 keV emission in many AGNs, combined with X-ray spectral timing and reverberation mapping, strongly indicates that the corona is physically compact, of the order 3–10 gravitational radii (Fabian et al. 2009, 2015; Kara et al. 2013; Emmanoulopoulos et al. 2014). The gravitational radius is defined to be $GM_{\rm BH}/c^2$, where $M_{\rm BH}$ is the supermassive black hole mass. Such radiatively compact sources can exchange significant energy between particles and photons, with the compactness characterized by the dimensionless parameter l (Guilbert et al. 1983), defined as

$$l = 4\pi \frac{m_p}{m_e} \frac{R_g}{R} \frac{L}{L_E}, \quad (1)$$

where m_p and m_e are the proton and electron mass, respectively, R_g is the gravitational radius, R is the source radius, L is the source luminosity, and $L_{\rm E}$ is the Eddington luminosity. The electron temperature T_e can also be characterized by the dimensionless parameter $\theta = k_{\rm B}T_e/m_ec^2$, where $k_{\rm B}$ is the Boltzmann constant. For sufficiently energetic photons, photon–photon collisions can lead to electron–positron pair production in the corona (Svensson 1982; Guilbert et al. 1983; Zdziarski 1985). At high coronal temperatures, when the Wien tail of the power-law spectrum extends above $2m_ec^2$, pair production can quickly become a runaway process, exceeding annihilation (Svensson 1984). This will limit any further rise in temperature, thus acting as an l-dependent thermostat (Svensson 1984; Zdziarski 1985; Stern et al. 1995).

The *NuSTAR* observatory (Harrison et al. 2013), being the first focusing hard X-ray telescope in orbit, has enabled detailed, high signal-to-noise spectra to be obtained in the 3–79 keV band for many local AGNs. *NuSTAR* spectral modeling can thus place constraints on the spectral photon index and high-energy cutoff of the coronal X-ray continuum, enabling robust estimates of l and θ. One of the primary goals of the *NuSTAR* mission is to perform an extragalactic survey of the hard X-ray sky in order to characterize the AGN population. We define hard X-rays as photons with energies >10 keV. As part of its Extragalactic Legacy Surveys program,[4] the *NuSTAR* observatory has performed snapshot ∼20 ks observations of local AGNs detected in the all-sky survey with the Burst Alert Telescope (BAT) instrument on board the *Neil Gehrels Swift Observatory* (Gehrels et al. 2004; Baumgartner et al. 2013). Though previous work has provided broad constraints on the high-energy cutoff for samples of bright AGNs, tight constraints for particular AGNs only became available recently thanks to *NuSTAR* (e.g., Ballantyne et al. 2014; Brenneman et al. 2014; Marinucci et al. 2014; Baloković et al. 2015; Fabian et al. 2015). The 100-fold increase in sensitivity of the *NuSTAR* telescope compared to the *Swift*/BAT instrument enables robust spectral modeling with a minimal *NuSTAR* exposure of ∼20 ks. With even longer exposure *NuSTAR* observations, it is possible to obtain tight limits on X-ray spectral parameters and perform reverberation mapping measurements of coronal size.

In this paper, we study a sample of 46 *Swift*/BAT-selected Seyfert 1 (Sy1) AGNs observed with *NuSTAR*, in order to map out the location of these sources on the temperature—compactness (θ–l) diagram for AGN coronae. We do not include *Swift*/XRT data in our spectral modeling as the limited data quality of available simultaneous *Swift*/XRT data introduces difficulties in obtaining constraints on parameters such as the cutoff energy. The complexity of features in soft X-ray spectra would ideally require high signal-to-noise ratio, simultaneous spectra from soft X-ray telescopes with larger collecting area to model robustly, which are currently unavailable for the targets in our sample. In Section 2, we discuss the sample used in this study, the data reduction, and

[4] https://www.nustar.caltech.edu/page/legacy_surveys

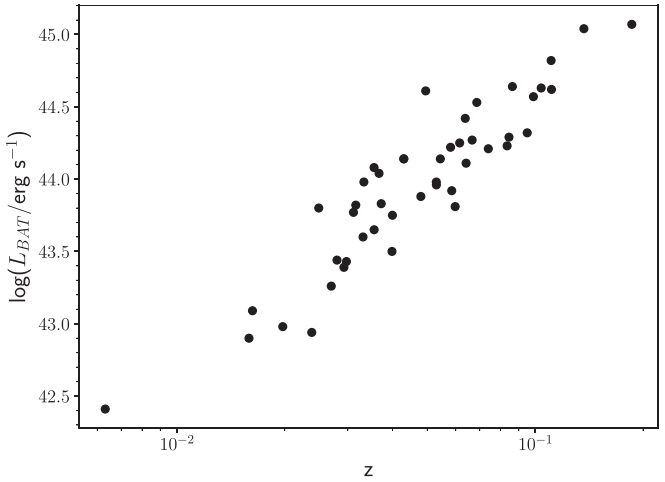

Figure 1. Redshift–luminosity distribution for *NuSTAR*-observed Sy1 AGNs selected from the *Swift*/BAT 70 month hard X-ray catalog.

analysis procedures adopted. Observational details of our AGN sample are presented in the Appendix. In Section 3, we present our results and discuss the heating and cooling mechanisms operating in the corona. We discuss future, deeper *NuSTAR* observations of AGNs in our sample with potential cutoffs in the *NuSTAR* band in Section 4, and present a summary in Section 5. In this work, all uncertainties were calculated at the 90% confidence level and standard values of the cosmological parameters ($h_0 = 0.7$, $\Omega_\Lambda = 0.7$, $\Omega_m = 0.3$) were used to calculate distances.

2. Sample, Data Reduction, and Analysis

2.1. Sample of Seyfert 1 AGNs

We selected our sample from AGNs identified in the *Swift*/BAT 70 month hard X-ray catalog (Gehrels et al. 2004; Baumgartner et al. 2013). From the full catalog, we selected *NuSTAR*-observed AGNs with known redshifts and classified as Sy1 from optical hydrogen emission line measurements, or from available data from the NASA/IPAC Extragalactic Database (NED). The full list of AGNs included in our study, along with their *NuSTAR* observation details, may be found in the Appendix. Figure 1 shows the location of our sources on the redshift–luminosity plane, with the luminosity values determined from the *Swift*/BAT fluxes in the 14–195 keV range. We confirmed sources at high redshift to not be beamed AGN or blazar candidates from observations of their optical spectra and cross-matching with the Roma Blazar Catalog (Massaro et al. 2009). We found two sources that were misclassified from NED and were removed from our sample. We excluded nine sources from our original sample due to lack of constraints on the high-energy cutoff from spectral fitting. Our final sample consists of 46 Sy1 AGNs at $0.003 < z < 0.2$.

In Figure 2, we present the distributions of *Swift*/BAT fluxes, luminosities, and redshifts for both our sample and the Sy1 classified sources from the *Swift*/BAT 70 month catalog. We find that our sample is statistically representative of the Sy1 population from the *Swift*/BAT 70 month catalog, with the mean and median values overlapping between our sample and the parent *Swift*/BAT sample. We further applied a two-sample Kolmogorov–Smirnov test and found the K–S test statistic to be 0.1 or lower, and the *p*-value above 60% for all three distributions, thus confirming that the distributions are consistent between our sample and the larger *Swift*/BAT sample of Sy1s.

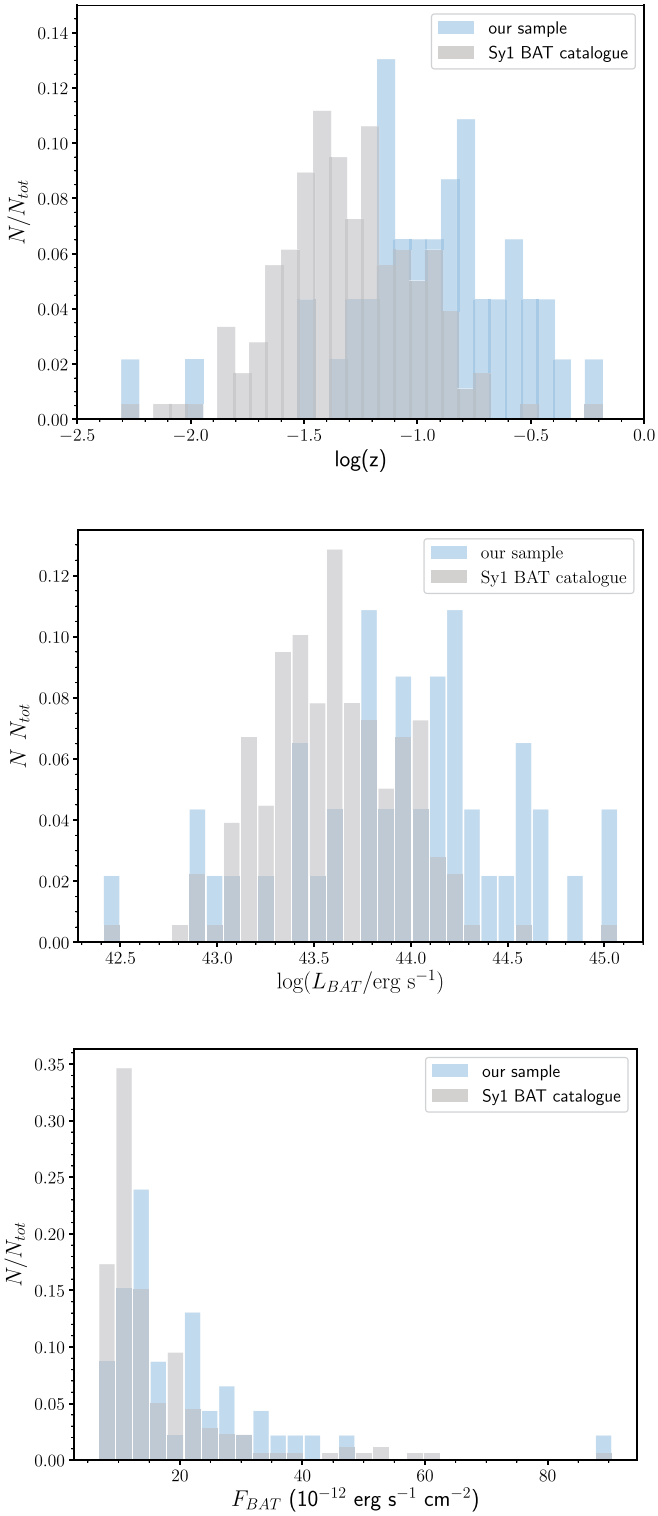

Figure 2. Distributions of redshifts, *Swift*/BAT 70 month X-ray catalog luminosities, and fluxes for both our sample and the Sy1 classified sources from the *Swift*/BAT catalog. For clarity, sources with $L_{\mathrm{BAT}} < 10^{40}$ erg s^{-1} and $F_{\mathrm{BAT}} > 1 \times 10^{-10}$ erg s^{-1} cm^{-2} were omitted from the plots.

2.2. NuSTAR Observations and Data Reduction

Roughly once per week since its start of science operations in 2013, the *NuSTAR* satellite has been obtaining ∼20 ks observations in the 3–79 keV band of AGNs selected from the *Swift*/BAT 70 month hard X-ray catalog (Baumgartner

et al. 2013). We performed reduction of raw event data from both *NuSTAR* modules, FPMA, and FPMB (Harrison et al. 2013), using the *NuSTAR* Data Analysis Software (NuSTARDAS; version 1.2.1), distributed by the NASA High Energy Astrophysics Archive Research Center (HEASARC) within the HEASOFT package (version 6.16). We took instrumental responses from the *NuSTAR* calibration database (CALDB; version 20160502). Raw event data were cleaned and filtered for South Atlantic Anomaly passages using the `nupipeline` module. We extracted source and background energy spectra from the calibrated and cleaned event files using the `nuproducts` module. Detailed information on these data reduction procedures can be found in the *NuSTAR* Data Analysis Software Guide (Perri et al. 2017). An extraction radius of 30″ was used for both the source and background regions. We extracted the background spectrum from source-free regions of the image, and away from the outer edges of the field of view, which have systematically higher background. The spectral files were rebinned using the HEASOFT task `grppha` to give a minimum of 20 photon counts per bin. For multiple observations of the same source, we coadded spectra using the HEASOFT task `addspec`.

2.3. Spectral Modeling

We performed spectral modeling of the *NuSTAR* data in the 3–79 keV band for each source in our sample using XSPEC v12.8.2 (Arnaud 1996). We used χ^2 statistics for all model fitting and error estimation. We adopted cross sections from Verner et al. (1996) and solar abundances from Wilms et al. (2000). In all our modeling we include a cross-correlation constant between FPMA and FPMB to account for slight differences in calibration (Madsen et al. 2015).

We fit each spectrum with an absorbed power-law model with a high-energy cutoff, $E_{\rm cut}$. The slope of the power-law continuum is characterized by the photon index, Γ. It is assumed that the intrinsic continuum intensity is proportional to $E^{-\Gamma}\exp(-E/E_{\rm cut})$. In XSPEC notation, the model used is `TBabs × zwabs × cutoffpl`, where the component `TBabs` models Galactic absorption, which is fixed to a typical Galactic column density of $7.6 \times 10^{21}\,{\rm cm}^{-2}$ (Kalberla et al. 2005). We found that freezing the Galactic column density did not have any significant effect on the fit results, as spectral modeling over the hard X-ray band is relatively insensitive to this parameter. The redshifted component `zwabs` accounts for absorption by the host galaxy.

Where an Fe Kα emission line feature was observed in the spectra at 6.4 keV, we added an additive `zgauss` Gaussian line component to the absorbed power-law model. We note that two objects out of our sample required fitting with an Fe Kα line: Mrk 595 and RBS 1037. In addition, we test for the presence of spectral features due to reprocessing by adding a `pexrav` component (Magdziarz & Zdziarski 1995). We fixed elemental abundances to solar and kept the inclination angle fixed at the default value of 60°. We found that the reduced χ^2 values and best-fit parameters from modeling with `pexrav` were similar to those from fitting an absorbed cutoff power-law for the majority of the sources in our sample, indicating that the addition of a reflection component does not significantly modify fit results and thus is not required by the data. Furthermore, we found that the null hypothesis probability exceeds 50% for many of our sources when fitting with an absorbed cutoff power-law; we found the mean null hypothesis probability of our sample to be 43%. We note that we chose a reflection model for one source (2MASX J19301380+3410495) due to best-fit parameters such as the photon index being more physically reasonable compared to the absorbed cutoff power-law model. We also note that the reduced χ^2 for Mrk 9 is relatively high due to increased scatter in the data near ∼10 and 30 keV, which do not correspond to any known physical features. We summarize some of the key best-fit spectral parameters for our sample in the Appendix. We did not find any sources in our sample with significant line-of-sight absorption ($>5 \times 10^{23}\,{\rm cm}^{-2}$), with most sources having hydrogen column densities constrained to be $<10^{22}\,{\rm cm}^{-2}$. Figure 3 presents an example *NuSTAR* spectrum for a potential low-cutoff candidate in our sample, 2MASX J19301380+3410495, for which we measured $E_{\rm cut}$ to be 23^{+29}_{-9} keV.

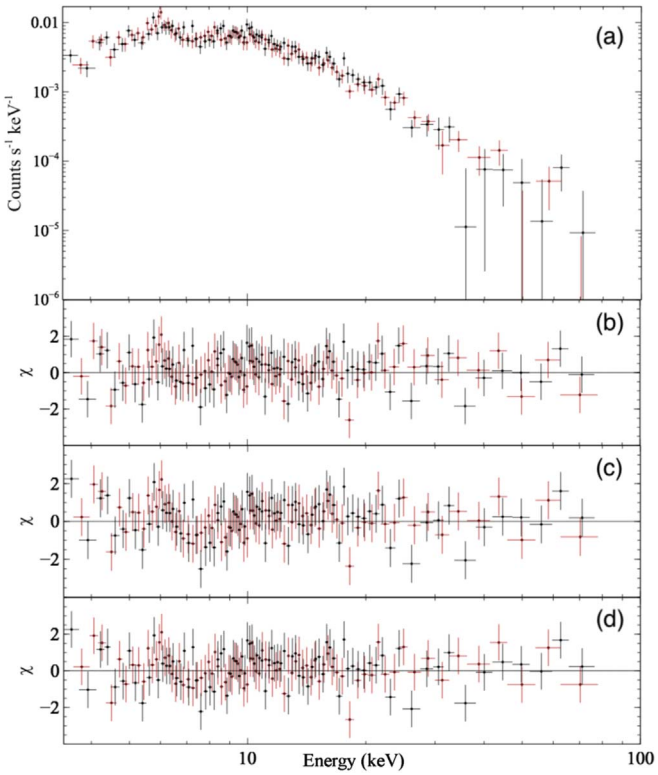

Figure 3. (a) *NuSTAR* hard X-ray spectrum of a candidate low-cutoff AGN 2MASX J19301380+3410495, alongside fit residuals for (b) an absorbed power-law model (χ^2/dof = 155.1/161), (c) an absorbed power-law model with a high-energy cutoff (χ^2/dof = 144.4/160), and (d) an absorbed cutoff power-law with reflection modeled via `pexrav` (χ^2/dof = 138/160). Black points correspond to FPMA data, while points in red correspond to FPMB.

3. Results and Discussion

In this section, we present limits on the high-energy cutoff, $E_{\rm cut}$, found from spectral modeling of our sample. We then present the location of our sources on the θ–l plane for AGN coronae and discuss the implications of sources with low values of $E_{\rm cut}$ on the heating and cooling mechanisms operating in the corona.

3.1. Cutoff Constraints

The distribution of lower limits on the high-energy cutoff for our sample is presented in Figure 4. The histogram shows a number of AGNs with lower limits on $E_{\rm cut}$ below 100 keV. Typical values of $E_{\rm cut}$ for AGNs generally range from ∼100 to 300 keV (Dadina 2007; Malizia et al. 2014; Ricci et al. 2017); we note that Gilli et al. (2007) comment that the mean value of

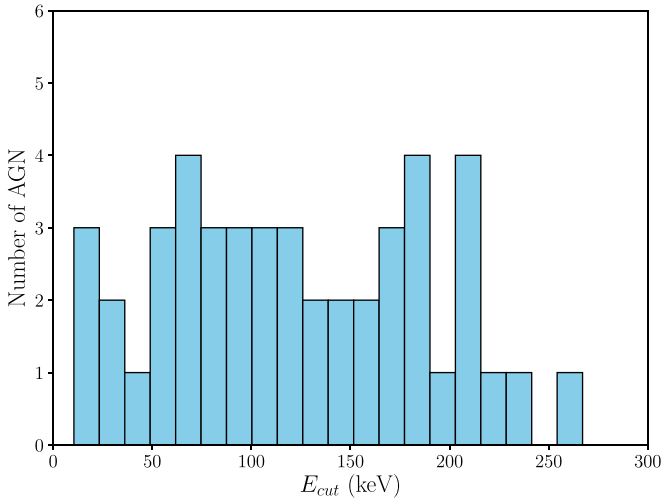

Figure 4. Distribution of lower limits on $E_{\rm cut}$ for our Sy1 AGN sample from modeling *NuSTAR* data.

$E_{\rm cut}$ for AGNs must not exceed several hundred keV in order to avoid overproducing the cosmic X-ray background above 100 keV.

Despite the fact that the quality of *NuSTAR* data in the hard X-ray band exceeds any previous observations of our targets, the cutoff power-law model does still display a degree of degeneracy in the derived photon index (Γ) and $E_{\rm cut}$. In order to verify that our constraints on $E_{\rm cut}$ are physically reasonable, in Figure 5 we compare our derived Γ and $E_{\rm cut}$ values to curves of constant optical depth in the $E_{\rm cut}$–Γ parameter space. The purple line in Figure 5 corresponds to theoretical constraints from Petrucci et al. (2001) for an optical depth $\tau = 6$. We use the relationship derived for a slab geometry of the corona by Petrucci et al. (2001) to calculate the optical depth as a function of Γ and $E_{\rm cut}$:

$$\Gamma = \sqrt{\frac{9}{4} + \frac{511\ \mathrm{keV}}{\tau kT_e(1+\tau/3)}} - \frac{1}{2}. \quad (2)$$

AGN coronae are typically thought to be optically thin ($\tau < 1$; Zdziarski 1985; Stern et al. 1995), though some have been constrained to $\tau \sim 3$ based on high-quality *NuSTAR* data (e.g., Baloković et al. 2015; Kara et al. 2017; Tortosa et al. 2017). Combinations of Γ and $E_{\rm cut}$ that correspond to $\tau > 6$ can be considered to result from a degeneracy between model parameters, and therefore are unphysical. With this particular assumption we suspect that for three targets our results may be unrealistic; if, for example, $\tau < 10$ is chosen, then no targets fall in this category. However, sources lying near or below the line with $\tau = 6$ were not removed from our sample, as the limited *NuSTAR* data quality with a short 20 ks exposure does not rule out physically reasonable values of the photon index.

We investigate the presence of model degeneracies in the sources with the lowest measured $E_{\rm cut}$ constraints (2MASX J19301380+3410495 and 1RXS J034704.9–302409) by exploring the $E_{\rm cut}$–Γ parameter space in XSPEC. Figure 6 shows the contour plots of the photon index against the high-energy cutoff for these sources. While there is some degree of degeneracy between these two parameters, the value of $E_{\rm cut}$ is constrained to low values over the range of physically reasonable photon index values at the 68% confidence level.

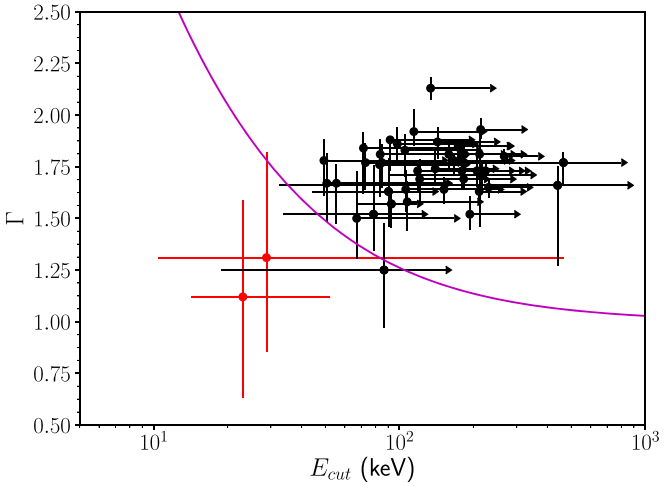

Figure 5. $E_{\rm cut}$ vs. photon index Γ for our sample. Points in red denote candidate sources with low coronal high-energy cutoffs for which both upper and lower limits on $E_{\rm cut}$ were measured. The purple line corresponds to theoretical constraints from Petrucci et al. (2001) for $\tau = 6$.

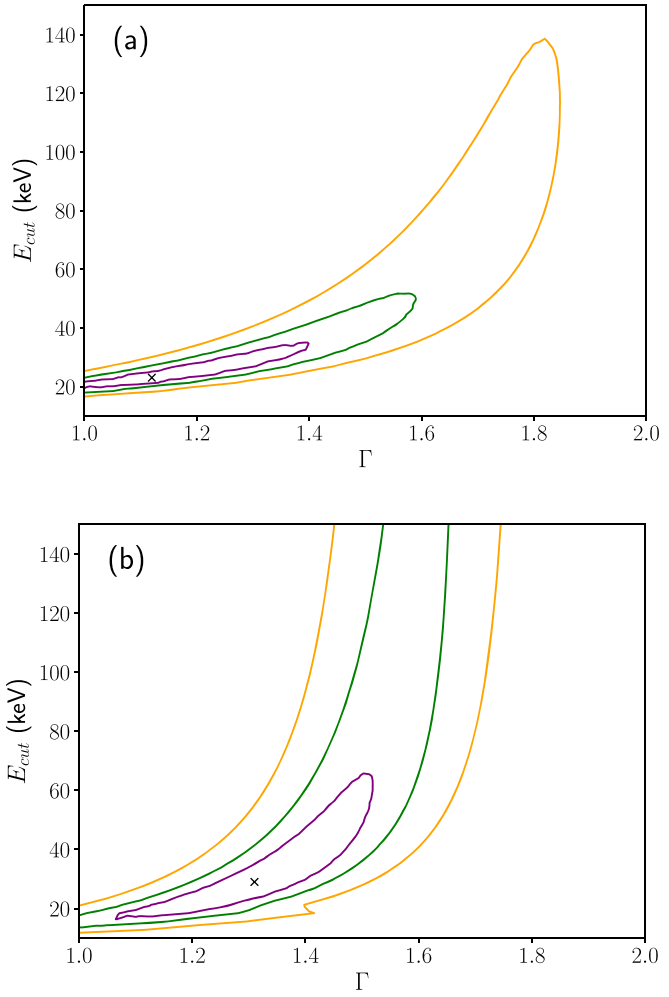

Figure 6. $E_{\rm cut}$–Γ contour plots for *NuSTAR* observations of the candidate low-cutoff Sy1s (a) 2MASX J19301380+3410495 and (b) 1RXS J034704.9–302409. The solid purple, green, and yellow contours correspond to the 68%, 90%, and 99% confidence levels, respectively. The black cross represents the best-fit values of the parameters from applying the relevant model given in the Appendix.

3.2. The θ–l Plane

In constructing the observational θ–l plane, we convert from $E_{\rm cut}$ to the coronal temperature using $k_{\rm B}T_e = E_{\rm cut}/2$ (Petrucci et al. 2001). In calculating l, we assume a conservative value of $10R_g$ for the coronal radius R, as adopted in Fabian et al. (2015), as the majority of the sources in our sample lack the required X-ray reflection modeling or reverberation measurements to place constraints on coronal size. We estimated the source luminosity L from the flux in the 0.1–200 keV band, which was extrapolated from the applied spectral model. We convert the unabsorbed 0.1–200 keV flux obtained from spectral modeling to luminosity using luminosity distance values from NED. Black hole mass estimates, where available, were taken from Koss et al. (2017). The values of $M_{\rm BH}$ used in Koss et al. (2017) were obtained from a combination of broad Balmer emission line measurements, direct techniques such as X-ray reverberation mapping, and the $M_{\rm BH}$–σ_* relation of Kormendy & Ho (2013). We have black hole mass measurements obtained from the literature for 34 of the 46 sources in our sample. For sources with no published black hole mass, we use the median black hole mass of the Sy 1–1.5 AGNs in the BAT AGN Spectroscopic Survey (BASS; Koss et al. 2017), $\log(M_{\rm BH}/M_\odot) = 7.97 \pm 0.52$.

We note that the precise location of AGNs on the θ–l plane is dependent on general relativistic effects, such as gravitational redshift and light bending. Processes such as light bending introduce inclination-dependent corrections to l. These corrections depend on the geometry of the corona, which is currently highly uncertain. Therefore, due to the large uncertainties associated with model-based relativistic corrections, we do not include general relativistic effects here.

Figure 7 presents the location of our sources on the θ–l plane, in addition to theoretical pair lines for different coronal geometries. Runaway pair production occurs to the right of the pair lines, as described in the introduction. Modeling the corona as an isolated electron cloud, Svensson (1984) estimated the pair production line to have the analytical form

$$l \sim 10\theta^{5/2}e^{1/\theta}. \quad (3)$$

Stern et al. (1995) also computed the pair balance line for a slab and hemispherical corona, respectively, located above a reflecting accretion disk. The solid black and purple lines in Figure 7 correspond to these geometries.

Our results show that most of the AGN coronae in our sample are clustered near the lines for runaway pair production, similar to the results found by Fabian et al. (2015) for *NuSTAR*-observed AGNs and black hole binaries. The pair lines thus appear to correspond to a physical boundary, constraining sources to that region. A few AGNs are located away from the pair line boundary, hinting at low coronal temperatures. Note that we have assumed that the corona is homogeneous and at a single temperature, whereas in reality there may be a range of temperatures. This may result in a mean temperature at a lower value due to Compton cooling (Fabian et al. 2015).

Recent detections of low coronal cutoffs have been made within the *NuSTAR* band, such as in Tortosa et al. (2017), Kara et al. (2017), and Xu et al. (2017). For example, Kara et al. (2017) measured $T_e = 15 \pm 2$ keV for the narrow-line Sy1 Ark 564, making it one of the lowest-temperature coronae observed by *NuSTAR* to date. Multiple explanations have been proposed for the origin of low-temperature coronae. In the case of an AGN accreting close to the Eddington limit, the stronger radiation field may enhance Compton cooling in comparison with sub-Eddington Seyferts (Kara et al. 2017). For sources accreting well below the Eddington limit, the relatively low coronal temperatures may be attributed to highly effective cooling in some AGNs due to, e.g., high spin and the resulting higher seed photon temperature. Low temperatures may also arise from particularly weak coronal heating mechanisms, or more effective cooling due to multiple scatterings in a corona with high optical depth (e.g., Tortosa et al. 2017). Naively, when the optical depth in the corona exceeds unity, multiple inverse Compton scatterings transfer a proportionally higher fraction of the stored thermal energy to coronal luminosity. However, coronae are complex systems, and many coupled physical processes determine the electron temperature.

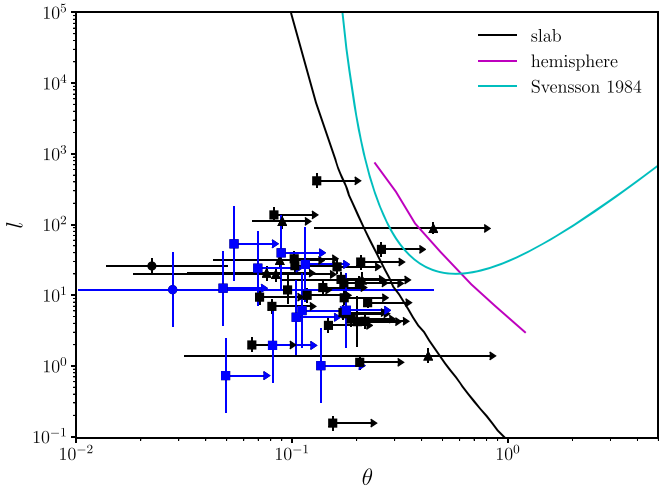

Figure 7. The θ–l plane for *NuSTAR*-observed Sy1 AGNs. Solid lines correspond to pair lines for different coronal geometries. Circled points are candidate low-cutoff sources for which both upper and lower limits on $E_{\rm cut}$ were measured. Triangles denote sources with a best-fit value and lower limit on $E_{\rm cut}$. Squares denote sources with only lower limits on $E_{\rm cut}$. Blue points indicate sources for which the black hole mass was taken to be the median black hole mass of the type 1 AGNs in the BAT AGN Spectroscopic Survey (BASS; Koss et al. 2017).

Another possibility is that the corona consists of a hybridized plasma, containing both thermal and nonthermal particles (e.g., Ghisellini et al. 1993; Zdziarski et al. 1993; Fabian et al. 2017). In such a system, the corona is highly magnetized and compact, and thus heating and cooling are so intense that electrons do not have time to thermalize before they are cooled by inverse Compton scattering. The presence of only a small fraction of nonthermal electrons with energies above 1 MeV can result in runaway pair production. The cooled electron–positron pairs may redistribute their available energy, thereby reducing the mean energy per particle and decreasing the coronal temperature. Such cooling would produce a hard nonthermal tail and an annihilation feature at 511 keV. Hard X-ray data of very high quality are necessary to distinguish between a hybrid, pair-dominated plasma and cooler, fully thermal plasma incapable of pair production.

4. Future Observations

The $E_{\rm cut}$ constraints presented here are based on snapshot ~20 ks *NuSTAR* observations of a sample of bright Sy1 galaxies and identified several sources that potentially have high-energy cutoffs within the *NuSTAR* band (i.e., 3–79 keV). Future work will involve performing longer exposure *NuSTAR*

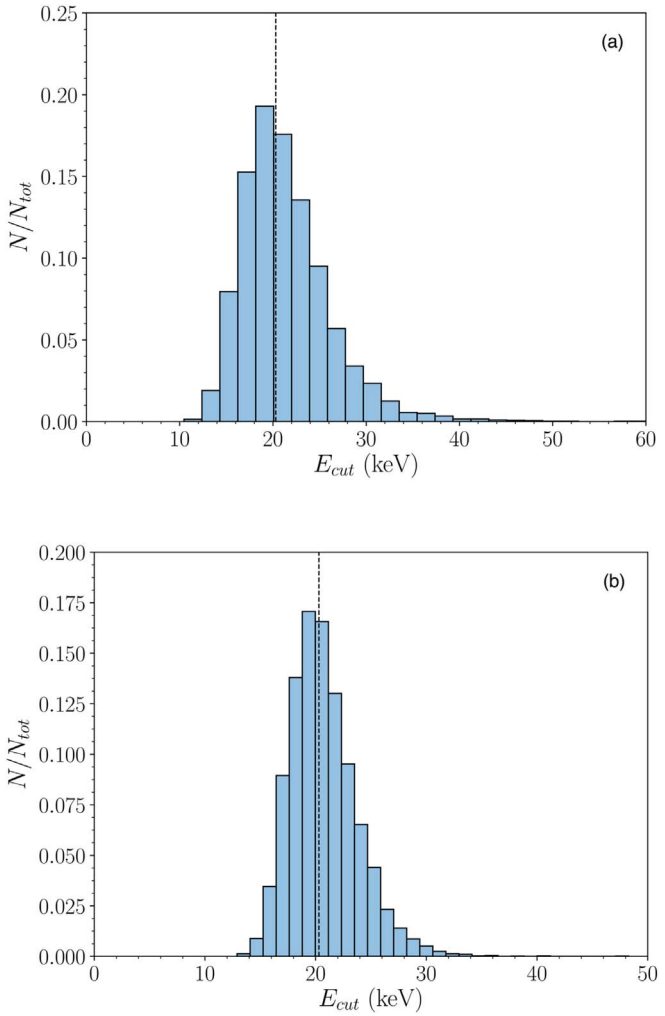

Figure 8. Distributions of $E_{\rm cut}$ values for 5000 simulations of the *NuSTAR* spectrum of a candidate low-cutoff AGN, 2MASX J19301380+3410495. Dotted lines denote the input $E_{\rm cut}$ value assumed for simulated spectra. Simulations were performed for exposure times of (a) 50 ks and (b) 100 ks.

observations of AGNs from our sample that display hints of a low coronal cutoff, which will aid in removing model degeneracies and more tightly constrain $E_{\rm cut}$ in order to determine the coronal temperature. In choosing AGNs from our sample for longer exposure *NuSTAR* observations, we performed 5000 simulations of the spectra of candidate low $E_{\rm cut}$ AGNs from our sample in XSPEC, for exposure times of 50 and 100 ks. From the simulated spectra, we plotted distributions of the best-fit value of $E_{\rm cut}$ found from applying an absorbed cutoff power-law model, in addition to lower limits and upper limits on $E_{\rm cut}$. The plots in Figure 8 show distributions of values of $E_{\rm cut}$ for one such candidate low-cutoff source, 2MASX J19301380+3410495. Table 1 summarizes the mean values of $E_{\rm cut}$ and its lower and upper limits obtained from our simulations for some candidate low-cutoff AGNs in our sample.

The simulation results show that the distributions peak at low values of $E_{\rm cut}$ and at similar values for both a 50 and 100 ks exposure. We conclude from our results that a 50 ks exposure should be sufficient to constrain the high-energy cutoff in our sample of candidate low-cutoff AGNs.

Table 1
Mean Values of the High-energy Cutoff and Its Lower and Upper Limits from Simulated *NuSTAR* Spectra, for *Swift*/BAT-selected Sy1 AGNs

Name	Exposure Time (ks)	$E_{\rm cut}$ (keV)	$E_{\rm cut}$ Lower Limit (keV)	$E_{\rm cut}$ Upper Limit (keV)
1RXS J034704.9–302409	50	92.7	17.1	118.8
	100	54.6	19.2	111.8
2MASX J19301380 +3410495	50	21.4	15.7	33.0
	100	20.7	16.7	27.0
Mrk 1393	50	189.0	43.5	191.7
	100	155.0	45.0	199.7
SDSS J104326d47 +110524.2	50	170.4	46.3	203.2
	100	134.1	52.1	206.5
UGC 06728	50	162.6	59.4	234.8
	100	127.5	67.6	222.8

5. Summary

In this work, we have investigated the coronal properties of a sample of *Swift*/BAT-selected Seyfert 1 AGNs that have been observed with *NuSTAR*. We individually modeled the *NuSTAR* spectra of all sources in our sample and searched for sources with hints of low coronal cutoffs, observable within the *NuSTAR* band. We mapped out the location of the sources in our sample on the compactness–temperature diagram for AGN coronae and found that the majority of sources lie near the boundary for runaway pair production. The pair production line corresponds to a physical boundary, constraining AGNs to that region. A few AGNs located away from the pair lines may possess low coronal temperatures; deeper 50 ks *NuSTAR* observations will be performed on these sources to constrain the coronal temperature and optical depth. The detection of low coronal cutoffs may be explained via scenarios such as a strong radiation field, large optical depth, or a hybrid pair-dominated plasma. Further computations with hybrid plasma models, taking into account general relativistic effects, will help elucidate in more detail the heating and cooling mechanisms operating in the corona.

We would like to thank the referee for comments that helped improve the final version of the manuscript. We have made use of data from the *NuSTAR* mission, a project led by the California Institute of Technology, managed by the Jet Propulsion Laboratory, and funded by the National Aeronautics and Space Administration. We thank the *NuSTAR* Operations, Software and Calibration teams for support with the execution and analysis of these observations. This research has made use of the *NuSTAR* Data Analysis Software (NuSTARDAS) jointly developed by the ASI Science Data Center (ASDC, Italy) and the California Institute of Technology (USA). M.B. acknowledges support from NASA Headquarters under the NASA Earth and Space Science Fellowship Program (grant NNX14AQ07H) and support from the black hole Initiative at Harvard University, through the grant from the John Templeton Foundation.

Facility: NuSTAR.

Appendix

We present the NuSTAR observation details and best-fit spectral parameters from fitting the NuSTAR data for our sample in Tables 2 and 3, respectively.

Table 2
NuSTAR Observation Details for *Swift*/BAT-selected Sy1 AGNs

Name	*Swift*/BAT ID	Observation ID	Observation Date	Exposure Time (ks)	Total Counts
1RXS J034704.9–302409	SWIFT J0347.0-3027	60061039002	2013 Mar 15	6.4	13.5
		60061039004	2013 Mar 24	12.7	20.4
		60061039006	2013 Apr 02	9.5	21.9
1RXS J174538.1+290823	SWIFT J1745.4+2906	60160674002	2014 Dec 09	20.3	2233
1RXS J213445.2–272551	SWIFT J2134.9−2729	60061306002	2013 Oct 22	19.8	2178
2MASS J19334715+3254259	SWIFT J1933.9+3258	60160714002	2016 May 31	12.6	3024
2MASX J04372814–4711298	SWIFT J0437.4−4713	60160197002	2015 Dec 09	20.0	1500
2MASX J12313717–4758019	SWIFT J1232.0−4802	60160498002	2016 Aug 21	19.3	1718
2MASX J15144217–8123377	SWIFT J1513.8−8125	60061263002	2013 Aug 06	13.3	1011
2MASX J15295830–1300397	SWIFT J1530.0−1300	60160617002	2017 Feb 14	24.2	2130
2MASX J19301380+3410495	SWIFT J1930.5+3414	60160713002	2016 Jul 19	20.5	1701
2MASX J19380437–5109497	SWIFT J1938.1−5108	60160716002	2016 Jul 15	21.8	2834
2MASX J20005575–1810274	SWIFT J2001.0−1811	60061295002	2016 Oct 25	21.9	1367
2MASXi J1802473–145454	SWIFT J1802.8−1455	60160680002	2016 May 01	20.0	6800
3C 227	SWIFT J0947.7+0726	60061329002	2014 Feb 20	17.2	293
		60061329004	2014 Feb 26	12.1	188
4C +18.51	SWIFT J1742.2+1833	60160672002	2017 Mar 27	22.5	1080
ESO 438–G009	SWIFT J1110.6−2832	60160423002	2015 Feb 01	21.7	1302
Fairall 1146	SWIFT J0838.4−3557	60061082002	2014 Jul 27	21.3	4473
Fairall 1203	SWIFT J0001.6−7701	60160002002	2015 Apr 11	34.1	1739
[HB89] 0241+622	SWIFT J0244.8+6227	60160125002	2016 Jul 31	23.4	9126
IGR J14471–6414	SWIFT J1446.7−6416	60061257002	2013 May 28	15.0	975
IGR J14552–5133	SWIFT J1454.9−5133	60061259002	2013 Sep 19	21.9	2190
IRAS 04392–2713	SWIFT J0441.2−2704	60160201002	2015 Dec 20	19.5	2145
LCRSB 232242.2–384320	SWIFT J2325.5−3827	60160826002	2016 Jul 08	22.5	495
Mrk 9	SWIFT J0736.9+5846	60061326002	2013 Oct 29	23.3	1142
Mrk 376	SWIFT J0714.3+4541	60160288002	2015 Apr 07	24.2	1791
Mrk 595	SWIFT J0241.6+0711	60160119002	2017 Jan 18	21.3	873
Mrk 732	SWIFT J1113.6+0936	60061208002	2013 Jun 11	26.3	3419
Mrk 739E	SWIFT J1136.0+2132	60260008002	2017 Mar 16	18.5	1277
Mrk 813	SWIFT J1427.5+1949	60160583002	2017 Jan 23	24.6	2952
Mrk 817	SWIFT J1436.4+5846	60160590002	2015 Jul 25	21.9	2847
Mrk 841	SWIFT J1504.2+1025	60101023002	2015 Jul 14	23.4	6084
Mrk 1018	SWIFT J0206.2−0019	60160087002	2016 Feb 10	21.6	583
Mrk 1044	SWIFT J0230.2−0900	60160109002	2016 Feb 08	21.7	2821
Mrk 1310	SWIFT J1201.2−0341	60160465002	2016 Jun 17	21.1	2743
Mrk 1393	SWIFT J1508.8−0013	60160607002	2016 Jan 19	22.4	896
NGC 0985	SWIFT J0234.6−0848	60061025002	2013 Aug 11	13.9	2363
PG 0804+761	SWIFT J0810.9+7602	60160322002	2016 Apr 02	17.3	1903
PKS 0558–504	SWIFT J0559.8−5028	60160254002	2016 Nov 19	21.0	2940
RBS 0295	SWIFT J0214.9−6432	60061021002	2017 Jan 14	23.3	1887
RBS 0770	SWIFT J0923.7+2255	60061092002	2012 Dec 26	18.9	6426
RBS 1037	SWIFT J1149.3−0414	60061215002	2017 Feb 02	40.7	2198
RBS 1125	SWIFT J1232.1+2009	60061229002	2016 Jul 28	20.0	1280
SBS 1136+594	SWIFT J1139.1+5913	60160443002	2014 Dec 26	23.5	3760
SDSS J104326.47+110524.2	SWIFT J1043.4+1105	60160406002	2016 Jun 14	20.1	137
UGC 06728	SWIFT J1143.7+7942	60160450002	2016 Jul 10	22.6	2486
UM 614	SWIFT J1349.7+0209	60160560002	2015 Mar 31	18.2	2002
WKK 1263	SWIFT J1241.6−5748	60160510002	2016 Apr 27	16.4	7872

Table 3
Redshifts, Black Hole Masses, and Best-fit Spectral Parameters from Fitting *NuSTAR* Data for Our *Swift*/BAT-selected Sy1 AGN Sample

Source	Redshift	$\log(M_{BH}/M_{\odot})$[a]	Γ	E_{cut} (keV)	$F_{0.1-200}$[b] 10^{-12} erg cm^{-2} s^{-1}	χ^2/dof	Model[c]
1RXS J034704.9–302409*	0.095	7.97 ± 0.52	$1.31^{+0.51}_{-0.46}$	29^{+437}_{-18}	$1.12^{+0.38}_{-0.10}$	50.9/50	1
1RXS J174538.1+290823	0.111	8.82 ± 0.10	$1.76^{+0.06}_{-0.16}$	$\geqslant 83$	$8.59^{+0.91}_{-0.89}$	181.5/187	1
1RXS J213445.2–272551	0.067	6.99 ± 0.10	$1.77^{+0.09}_{-0.12}$	$\geqslant 85$	$7.62^{+0.73}_{-0.38}$	155.8/175	1
2MASS J19334715+3254259	0.057	7.88 ± 0.10	$1.78^{+0.04}_{-0.06}$	$\geqslant 166$	$15.3^{+0.6}_{-0.6}$	236.3/225	1
2MASX J04372814–4711298*	0.053	7.97 ± 0.52	$1.92^{+0.11}_{-0.07}$	$\geqslant 114$	$5.08^{+0.56}_{-0.25}$	147.5/123	1
2MASX J12313717–4758019*	0.028	7.97 ± 0.52	$1.81^{+0.07}_{-0.12}$	$\geqslant 84$	$5.88^{+0.75}_{-0.46}$	107.8/139	1
2MASX J15144217–8123377	0.068	8.96 ± 0.10	$1.66^{+0.09}_{-0.39}$	$\geqslant 32$	$6.67^{+0.94}_{-1.24}$	95.3/86	1
2MASX J15295830–1300397*	0.104	7.97 ± 0.52	$1.73^{+0.04}_{-0.10}$	$\geqslant 119$	$5.49^{+0.25}_{-0.25}$	172.4/170	1
2MASX J19301380+3410495	0.063	8.15 ± 0.10	$1.12^{+0.47}_{-0.49}$	23^{+29}_{-9}	$22.9^{+5.98}_{-3.77}$	138/160	2
2MASX J19380437–5109497	0.040	7.23 ± 0.10	$1.83^{+0.08}_{-0.12}$	$\geqslant 105$	$9.03^{+0.78}_{-0.65}$	214.2/215	1
2MASX J20005575–1810274	0.037	8.07 ± 0.36	$1.73^{+0.08}_{-0.08}$	$\geqslant 207$	$9.62^{+0.79}_{-0.76}$	285.1/250	1
2MASXi J1802473–145454	0.003	7.76 ± 0.10	$1.81^{+0.05}_{-0.07}$	$\geqslant 159$	$23.9^{+1.3}_{-1.2}$	466.3/451	1
3C 227	0.086	8.61 ± 0.10	$1.63^{+0.16}_{-0.17}$	$\geqslant 44$	$11.7^{+1.1}_{-0.9}$	331/347	1
4C +18.51*	0.186	7.97 ± 0.52	$1.67^{+0.09}_{-0.19}$	$\geqslant 55$	$3.04^{+0.34}_{-0.20}$	73.2/100	1
ESO 438–G009*	0.024	7.97 ± 0.52	$1.74^{+0.09}_{-0.07}$	$\geqslant 140$	$3.95^{+0.23}_{-0.23}$	92.3/113	1
Fairall 1146*	0.031	7.97 ± 0.52	$1.81^{+0.04}_{-0.05}$	$\geqslant 184$	$14.1^{+0.9}_{-0.5}$	365.9/326	1
Fairall 1203*	0.058	7.97 ± 0.52	$1.58^{+0.11}_{-0.07}$	$\geqslant 108$	$3.37^{+0.38}_{-0.33}$	139.4/150	1
[HB89] 0241+622	0.044	8.09 ± 0.10	$1.63^{+0.04}_{-0.05}$	$\geqslant 211$	$24.1^{+1.0}_{-7.4}$	631.1/565	1
IGR J14471–6414	0.053	7.70 ± 0.10	$1.77^{+0.09}_{-0.13}$	$\geqslant 73$	$4.08^{+0.51}_{-0.28}$	84.3/82	1
IGR J14552–5133	0.016	6.86 ± 0.10	$1.73^{+0.03}_{-0.09}$	$\geqslant 180$	$6.43^{+0.35}_{-0.25}$	191.9/181	1
IRAS 04392–2713*	0.084	7.97 ± 0.52	$1.84^{+0.08}_{-0.22}$	$\geqslant 71$	$7.82^{+0.71}_{-0.44}$	200.8/173	1
LCRSB 232242.2–384320*	0.036	7.97 ± 0.52	$1.67^{+0.14}_{-0.19}$	$\geqslant 51$	$1.44^{+0.20}_{-0.13}$	50.9/46	1
Mrk 9	0.040	7.59 ± 0.10	$1.52^{+0.08}_{-0.08}$	$\geqslant 193$	$2.83^{+0.19}_{-0.18}$	155.1/100	1
Mrk 376	0.056	8.17 ± 0.10	$1.64^{+0.06}_{-0.07}$	$\geqslant 152$	$4.38^{+0.37}_{-0.20}$	170.3/147	1
Mrk 595	0.027	8.28 ± 0.10	$1.50^{+0.23}_{-0.20}$	$\geqslant 67$	$2.62^{+0.43}_{-0.33}$	79.5/76	3
Mrk 732	0.029	7.23 ± 0.10	$1.85^{+0.07}_{-0.07}$	$\geqslant 173$	$7.95^{+0.31}_{-0.31}$	269.6/258	1
Mrk 739E	0.030	7.14 ± 0.10	$1.87^{+0.07}_{-0.08}$	$\geqslant 143$	$4.80^{+0.30}_{-0.29}$	113.1/106	1
Mrk 813	0.110	8.87 ± 0.10	$1.85^{+0.03}_{-0.10}$	$\geqslant 177$	$7.95^{+0.31}_{-0.31}$	269.6/230	1
Mrk 817	0.031	7.59 ± 0.07	$1.65^{+0.04}_{-0.05}$	$\geqslant 230$	$7.82^{+0.36}_{-0.30}$	263.1/214	1
Mrk 841	0.036	7.81 ± 0.10	$1.78^{+0.05}_{-0.06}$	$\geqslant 179$	$17.9^{+1.0}_{-0.7}$	403.9/425	1
Mrk 1018	0.042	8.03 ± 0.10	$1.81^{+0.14}_{-0.35}$	$\geqslant 212$	$1.76^{+0.46}_{-0.24}$	50.5/51	1
Mrk 1044	0.016	6.44 ± 0.10	$1.93^{+0.05}_{-0.05}$	$\geqslant 214$	$8.74^{+0.36}_{-0.36}$	215.2/205	1
Mrk 1310	0.019	6.21 ± 0.08	$1.77^{+0.05}_{-0.10}$	$\geqslant 130$	$8.68^{+0.72}_{-0.32}$	215/217	1
Mrk 1393	0.054	7.87 ± 0.10	$1.25^{+0.23}_{-0.28}$	$\geqslant 19$	$2.07^{+0.47}_{-0.21}$	109.8/79	1
NGC 0985	0.043	7.92 ± 0.10	$1.69^{+0.10}_{-0.11}$	$\geqslant 121$	$11.7^{+1.1}_{-0.97}$	187/195	1
PG 0804+761	0.100	8.73 ± 0.05	$1.69^{+0.07}_{-0.05}$	$\geqslant 183$	$6.85^{+0.34}_{-0.33}$	126.3/155	1
PKS 0558–504	0.137	7.33 ± 0.10	$2.13^{+0.05}_{-0.06}$	$\geqslant 134$	$10.4^{+3.7}_{-0.39}$	217.9/206	1
RBS 0295*	0.074	7.97 ± 0.52	$1.78^{+0.10}_{-0.17}$	$\geqslant 49$	$5.32^{+0.51}_{-0.42}$	149.3/153	1
RBS 0770	0.032	7.34 ± 0.10	$1.80^{+0.03}_{-0.03}$	$\geqslant 267$	$22.8^{+0.59}_{-0.58}$	400.3/434	1
RBS 1037*	0.084	7.97 ± 0.52	$1.88^{+0.01}_{-0.15}$	$\geqslant 92$	$3.77^{+0.17}_{-0.19}$	180.6/185	3
RBS 1125	0.063	7.76 ± 0.20	$1.86^{+0.08}_{-0.10}$	$\geqslant 98$	$4.11^{+0.25}_{-0.25}$	109.1/107	1
SBS 1136+594	0.060	7.98 ± 0.10	$1.71^{+0.06}_{-0.08}$	$\geqslant 92$	$10.6^{+0.4}_{-0.4}$	295/285	1
SDSS J104326.47+110524.2	0.048	7.91 ± 0.10	$1.52^{+0.24}_{-0.18}$	$\geqslant 34$	$4.13^{+0.69}_{-0.23}$	122/122	1
UGC 06728	0.006	5.66 ± 0.10	$1.57^{+0.07}_{-0.11}$	$\geqslant 67$	$6.96^{+0.30}_{-0.30}$	227.3/208	1
UM 614	0.033	7.09 ± 0.10	$1.64^{+0.09}_{-0.11}$	$\geqslant 106$	$7.31^{+0.71}_{-0.50}$	162.7/172	1
WKK 1263	0.024	8.25 ± 0.10	$1.73^{+0.04}_{-0.04}$	$\geqslant 224$	$31.6^{+1.5}_{-1.1}$	470.3/503	1

Notes. Sources marked with an asterisk (*) correspond to AGNs whose black hole masses were taken to be the median black hole mass of the type 1 AGNs in the BAT AGN Spectroscopic Survey (BASS; Koss et al. 2017).
[a] Koss et al. (2017).
[b] Unabsorbed 0.1–200 keV flux extrapolated from the applied spectral model.
[c] Applied XSPEC models: (1) `constant × TBabs × zwabs × cutoffpl`, (2) `constant × TBabs × zwabs × (cutoffpl + pexrav)`, and (3) `constant × TBabs × zwabs × (cutoffpl + zgauss)`.

ORCID iDs

N. Kamraj https://orcid.org/0000-0002-3233-2451
F. A. Harrison https://orcid.org/0000-0003-2992-8024
M. Baloković https://orcid.org/0000-0003-0476-6647

References

Arnaud, K. 1996, in ASP Conf. Ser. 101, Astronomical Data Analysis Software and Systems, ed. G. H. Jacoby & J. Barnes (San Francisco, CA: ASP), 17
Ballantyne, D. R., Bollenbacher, J. M., Brenneman, L. W., et al. 2014, ApJ, 794, 62
Baloković, M., Matt, G., Harrison, F. A., et al. 2015, ApJ, 800, 62
Baumgartner, W. H., Tueller, J., Markwardt, C. B., et al. 2013, ApJS, 207, 19
Brenneman, L. W., Madejski, G., Fuerst, F., et al. 2014, ApJ, 781, 83
Dadina, M. 2007, A&A, 461, 1209
Emmanoulopoulos, D., Papadakis, I. E., Dovčiak, M., & McHardy, I. M. 2014, MNRAS, 439, 3931
Fabian, A. C., Lohfink, A., Belmont, R., Malzac, J., & Coppi, P. 2017, MNRAS, 467, 2566
Fabian, A. C., Lohfink, A., Kara, E., et al. 2015, MNRAS, 451, 4375
Fabian, A. C., Zoghbi, A., Ross, R. R., et al. 2009, Natur, 459, 540
Gehrels, N., Chincarini, G., Giommi, P., et al. 2004, ApJ, 611, 1005
Ghisellini, G., Haardt, F., & Fabian, A. C. 1993, MNRAS, 263, 9
Gilli, R., Comastri, A., & Hasinger, G. 2007, A&A, 463, 79
Guilbert, P. W., Fabian, A. C., & Rees, M. J. 1983, MNRAS, 205, 593
Haardt, F., & Maraschi, L. 1993, ApJ, 413, 507
Harrison, F. A., Craig, W. W., Christensen, F. E., et al. 2013, ApJ, 770, 103
Kalberla, P. M. W., Burton, W. B., Hartmann, D., et al. 2005, A&A, 440, 775
Kara, E., Fabian, A. C., Cackett, E. M., Miniutti, G., & Uttley, P. 2013, MNRAS, 430, 1408
Kara, E., García, J. A., Lohfink, A., et al. 2017, MNRAS, 468, 3489
Kormendy, J., & Ho, L. C. 2013, ARA&A, 51, 511
Koss, M., Trakhtenbrot, B., Ricci, C., et al. 2017, ApJ, 850, 74
Madsen, K. K., Harrison, F. A., Markwardt, C. B., et al. 2015, ApJ, 220, 8
Magdziarz, P., & Zdziarski, A. A. 1995, MNRAS, 273, 837
Malizia, A., Molina, M., Bassani, L., et al. 2014, ApJL, 782, L25
Marinucci, A., Matt, G., Miniutti, G., et al. 2014, ApJ, 787, 83
Massaro, E., Giommi, P., Leto, C., et al. 2009, A&A, 495, 691
Perri, M., Puccetti, S., Spagnuolo, N., et al. 2017, The NuSTAR Data Analysis Software Guide v1.9.3, https://heasarc.gsfc.nasa.gov/docs/nustar/analysis/nustar_swguide.pdf
Petrucci, P. O., Haardt, F., Maraschi, L., et al. 2001, ApJ, 556, 716
Ricci, C., Trakhtenbrot, B., Koss, M. J., et al. 2017, ApJS, 233, 17
Rybicki, G. B., & Lightman, A. P. 1979, Radiative Processes in Astrophysics (New York: Wiley-Interscience)
Stern, B. E., Poutanen, J., Svensson, R., Sikora, M., & Begelman, M. C. 1995, ApJL, 449, L13
Svensson, R. 1982, ApJ, 258, 335
Svensson, R. 1984, MNRAS, 209, 175
Tortosa, A., Marinucci, A., Matt, G., et al. 2017, MNRAS, 466, 4193
Verner, D. A., Ferland, G. J., Korista, K. T., & Yakovlev, D. G. 1996, ApJ, 465, 487
Wilms, J., Allen, A., & McCray, R. 2000, ApJ, 542, 914
Xu, Y., Baloković, M., Walton, D. J., et al. 2017, ApJ, 837, 21
Zdziarski, A. A. 1985, ApJ, 289, 514
Zdziarski, A. A., Poutanen, J., & Johnson, W. N. 2000, ApJ, 542, 703
Zdziarski, A. A., Zycki, P. T., & Krolik, J. H. 1993, ApJL, 414, L81